Differential cavity ring-down spectroscopy

Jérémie Courtois,[1] Katarzyna Bielska,[1,2] and Joseph T. Hodges[1,*]

[1]*Chemical Sciences Division, National Institute of Standards and Technology, 100 Bureau Drive, Gaithersburg, Maryland 20899, USA*

[2]*Institute of Physics, Faculty of Physics, Astronomy and Informatics, Nicolaus Copernicus University, Grudziadzka 5, 87-100 Toruń, Poland*

**Corresponding author: joseph.hodges@nist.gov*

Received December 19, 2012; revised February 19, 2013; accepted March 7, 2013; posted April 11, 2013 (Doc. ID 181954); published May 9, 2013

High-precision cavity-enhanced spectroscopic measurements are commonly compromised by interferences caused by external etalons. Here, we present the differential cavity ring-down spectroscopy (D-CRDS) technique for reducing these perturbations. We discuss how etalons are caused by coupled-cavity interactions between the primary ring-down cavity and other optical elements of the experiment, and we model and experimentally verify how drift in cavity base loss correlates with barometric pressure and laboratory temperature. D-CRDS measurements of near-infrared CO_2 spectra that are insensitive to etalon-induced distortions are then presented. Based on an average of ~100 spectra, these results yield a signal-to-noise ratio of 170,000:1 and a minimum detectable absorption coefficient of 4×10^{-12} cm^{-1}.

OCIS codes: (120.6200) Spectrometers and spectroscopic instrumentation; (300.6360) Spectroscopy, laser; (300.6390) Spectroscopy, molecular.

http://dx.doi.org/10.1364/JOSAB.30.001486

1. INTRODUCTION

The use of optical resonators comprising ultra-high-reflectivity mirrors enables a wide variety of cavity-enhanced absorption spectroscopy techniques for which extremely long optical path lengths and, hence, high sensitivity are achieved [1]. However, uncontrolled variations in base losses of the cavity that are caused by spurious reflections [2] or by etalon/coupled-cavity effects [3] usually complicate measured spectra. These perturbations (typically referred to as etaloning) are caused by self-mixing between the circulating intracavity light and the external light that recouples through a cavity mirror port. For example, in early cavity ring-down spectroscopy (CRDS) experiments, sinusoidal variations in the base losses were ascribed to etaloning arising from the back surface of ring-down cavity (RDC) mirrors [4]. Etaloning causes the reflectivity of the involved resonator mirror to depend on the phase (i.e., wavelength and path length), amplitude, and spatial coupling efficiency of the recoupled field, leading to an effective mirror reflectivity that can be significantly greater or less than that of the isolated mirror [3]. Although etaloning recently was demonstrated as a potentially beneficial mechanism that enables active control of the cavity finesse [3], this effect usually is undesirable because it causes uncertainty in the spectrometer's base losses. Indeed this effect typically sets a lower bound on the spectrometer detection limit, especially for long averaging times. However, the amplitude of etalons in measured baselines can be reduced by long-term averaging, most likely because of stochastic variations in the etalon phase [5–7]. In the case of high fidelity line shape measurements, distortion caused by drifting etalons is commonly reduced by subtracting (fitting) baselines that comprise one or more sinusoidal components from (to) measured spectra. When long-term measurements are implemented, drift in the cavity base losses usually makes such postcorrections unreliable unless the time-varying etalon phase and amplitude are taken into account [8].

Ideally, and in the absence of scattering, an etalon-free cavity-enhanced spectrometer would be achieved by tilting all the optical interfaces traversed by the light with respect to the cavity's optical axis. In this manner, all specular reflections that retroreflect the leaking RDC mode would be suppressed. This requires careful alignment (note that the use of antireflective coatings on all optical elements of a cavity-enhanced setup is a prerequisite under normal experimental conditions). However, as shown below, for experiments involving high-finesse cavities, even residual feedback at the part-per-thousand intensity scale can significantly influence the base losses. Complete elimination of etalons in high-finesse cavity-enhanced spectrometers is, thus, rarely if ever realized. A recent exception is a high-sensitivity, long-term averaging CRDS study, in which the authors report no direct evidence of etaloning [7]. However, we note (unlike the measurements herein) that these measurements involve continuous dithering of the RDC length, an approach that diminishes the contributions of etalons (on the side of the moving mirror) at the expense of reduced spectrum frequency resolution. Another approach to suppressing the effects of residual etalons would be to capture at a given time the spectral dependence of the absorption-free baseline by alternating between measurements of samples with and without the analyte. In this sample modulation approach, the measured etalon could be, in principle, subtracted from the absorption spectrum. This method has been implemented in a noncavity-enhanced spectrometer in which the system was alternately flushed using gas mixtures with and without the absorbing species for recording background spectra [9]. This approach to sample modulation for recording reference spectra is

limited by the relatively slow refresh rate of the gas sample. Also, for completeness, we mention that sample modulation has been realized via the Stark effect in a nonresonant multipass absorption cell [10]. In this fashion an alternating electric field was used to separate background and absorption losses.

In cavity-enhanced spectrometers, etalon fringes have been reduced by subtracting background spectra [11] or by installing elements at so-called etalon-immune distances [12], which correspond to multiples of $c/(2\nu_m)$ where c is the speed of light and ν_m is the laser modulation frequency. Note that the cavity free spectral range (FSR) is given by $c/(2l_c)$, where l_c is the RDC length. Indeed, when sources of optical feedback are placed at distances that equal a multiple or submultiple of l_c, the etalon modulation amplitude in the resulting spectrum is suppressed. This results because the sinusoidal etalon is sampled at optical frequencies that correspond to a constant etalon phase. Nevertheless, the method requires that the optical items traversed by the light be accurately located since any mismatch in the previous condition incurs undesired aliasing of the modulation. Further, this method does not address the issue of baseline drift, namely the etalon phase shifts that occur under normal experimental conditions.

In the present study we present a new approach to CRDS [13] that enables reduction in the etalon-induced variations in base RDC losses, including diminution of drift-related effects. The idea was inspired by two previous CRDS methods [14,15] that relied on the rapid alternation and acquisition of on- and off-absorption line measurements with two laser beams having different frequencies: our present idea is to scan both frequencies together and evaluate the difference spectrum. To demonstrate, we alternately measure and then subtract intracavity losses associated with pairwise TEM_{00} modes that are separated in frequency by an integer value, Δq, of the RDC FSR. Each measurement pair is acquired rapidly enough to overcome the effects of etalon drift. We call this technique differential CRDS (D-CRDS). Importantly, we note that the present study corresponds to a length-stabilized RDC (with no mirror dithering) that has a frequency resolution and long-term stability of ~1 MHz [16]. As shown below, the etalon phases drift because of temperature- and pressure-dependence of external pathlengths, despite the fact that the RDC itself is length-stabilized. To mitigate the effect of etalons, we demonstrate that specific placements of the optical elements relative to the high-reflectivity surfaces of the RDC mirrors correspond to etalon-reduced regions (ERRs). This configuration can lead to improved measurement performance when the differential method is applied. For scans through an absorption line, the resulting D-CRDS technique yields spectra with substantially higher signal-to-noise ratios (SNRs) than those of a conventional CRDS spectra. This improved performance is caused by reduction of the etalon amplitude (which tends to reduce the effects of etalon drift, thus minimizing distortion of average spectra acquired over long time intervals) and by an enhancement of the magnitude of the absorption profile. Importantly, no additional fitting parameters are required to fit line shape models to D-CRDS spectra.

In the remainder of this article we model cavity ring-down spectra that exhibit etaloning effects and we show how a differencing approach can alter the magnitude of these etalons. Subsequently, we present D-CRDS measurements of empty cavity losses in which we demonstrate reduced sensitivity to drift in etalon amplitude and phase. A model is then derived, highlighting how slow drift in cavity base losses correlates with measured barometric pressure and laboratory temperature. Finally, to illustrate the performance of this technique, we present and compare D-CRDS and frequency-stabilized CRDS (FS-CRDS) [16,17] measurements of a CO_2 absorption line near 6246.3 cm^{-1}. For brevity, hereafter when referring to the "conventional CRDS" technique we mean FS-CRDS (not to be confused with more common implementations of CRDS that use unstabilized ring-down cavities). We also include an Appendix where we model coupled-cavity effects that induce variations in RDC base losses, and where we introduce the concept of ERRs that must be considered for optimization of the D-CRDS technique.

2. PRINCIPLE, EXPERIMENTAL PROCEDURES, AND MEASUREMENTS

A. Spectrum Model

When cavity CRDS is implemented with a length-stabilized cavity (i.e., FS-CRDS method), the decay time τ is measured at regularly spaced values of the optical frequency ν. The reciprocal of the decay time (decay rate) can be modeled as the sum of all system optical losses, including absorption by the cavity medium and the effective mirror losses. In practice, etalons are manifest by sinusoidal, frequency-dependent variation in the mirror losses. Defining the total RDC loss-per-unit length as $1/(c\tau)$ and summing over N etalons gives

$$\frac{1}{c\tau_j} = \alpha_a(\nu_j) + \alpha_m + \sum_i^N \Delta\alpha_{e,i} \sin\left(\frac{2\pi\nu_j}{\nu_{e,i}} + \phi_i(t)\right) \quad (1)$$

for the jth point in an FS-CRDS spectrum. In this formula, the τ_j and ν_j terms are measured quantities; α_a is the absorption loss within the RDC medium; α_m is the base loss in the absence of etaloning; and $\Delta\alpha_{e,i}$, $\nu_{e,i}$, and ϕ_i are the amplitude, period, and phase of the ith etalon, respectively. We assume α_m to be given by $(1-R)/l_c$ where R is the intensity reflectivity of the RDC mirrors, which for simplicity we assume to be constant. Note that in order to account for small changes in optical path lengths that perturb the etalons, we explicitly indicate time dependence in the etalon phases through the independent variable t. In Appendix A we present generalized relationships for the effective base loss of the system as a function of the reflectivity, the transmittance, path lengths, and spatial coupling coefficients for an arbitrary number of external optical elements that form coupled cavities with the RDC. For weak coupling with a high-finesse RDC, the contribution of each coupled cavity essentially reduces to a sinusoidal term as given in the summation of Eq. (1).

The D-CRDS method described here gives the following spectrum that we note is independent of α_m:

$$\begin{aligned}\Delta\alpha(\nu_j) = {} & \alpha_a(\nu_j + \Delta\nu) - \alpha_a(\nu_j - \Delta\nu) \\ & + \sum_i^N \Delta\alpha_{e,i}\left[\sin\left(\frac{2\pi(\nu_j + \Delta\nu)}{\nu_{e,i}} + \phi_i\right)\right. \\ & \left. - \sin\left(\frac{2\pi(\nu_j - \Delta\nu)}{\nu_{e,i}} + \phi_i\right)\right], \end{aligned} \quad (2)$$

where ν_j is the unshifted laser frequency and $\Delta\nu = \Delta q \times \mathrm{FSR}/2$. Evaluation of the sinusoidal terms in Eq. (2) reveals that the differential spectrum can either suppress or amplify a specific etalon amplitude, depending on the ratio $\Delta\nu/\nu_e$. Specifically, the etaloning terms cancel if $2\Delta\nu/\nu_e = k$, where k is an integer. Conversely, for the ratio $2\Delta\nu/\nu_e = m/2$, where m is an odd integer, the two terms are out of phase and give an amplitude of $2\Delta\alpha_e$, corresponding to an amplification factor of 2. For $\Delta q = 2$ and $k = 1$ or $m = 3$, then these two limiting cases correspond to $l_e/l_c = 1/2$ and $l_e/l_c = 3/4$, respectively, where l_e/l_c is the ratio of etalon length to cavity length. Arbitrary values of $\Delta\nu/\nu_e$ result in an amplification factor between 0 and 2 and, consequently, the values of Δq and ν_e must be chosen to ensure that the D-CRDS technique reduces the etalon amplitude. A generalized analysis of this amplification factor is given in the Appendix B.

B. The Differential Technique: Experimental Apparatus and Measurements of Empty Cavity Base Losses

To demonstrate the D-CRDS approach for reduction of etaloning effects, we use an FS-CRDS apparatus [17] consisting of a 74 cm long, two-mirror length-stabilized RDC with $R \sim 99.998\%$ [$T = (1 - R) \sim 2 \times 10^{-5}$]. The high-reflectivity mirrors comprise multilayer stack (MLS) dielectric coatings on fused silica substrates that have a radius of curvature of 1 m. We use a distributed feedback (DFB) semiconductor diode fiber-coupled laser emitting near the wavelength of $\lambda = 1.6$ μm for our probe beam. The probe laser is effectively switched off using a semiconductor amplifier [booster optical amplifier (BOA)] that is externally triggered and used to initiate the ring-down decay events. As depicted in Fig. 1, the principal novelty of this experiment relies on utilizing two fiber-pigtailed variable-frequency (tuning range of 20 MHz) acousto-optic modulators (AOMs). These are driven by two switchable radio-frequency (RF) sources, each with a 50 dB extinction ratio. The AOM devices have two functions. First, they act as optical switches to select each probe beam. Second, the AOMs act as frequency shifters for each probe beam. They are designed so that AOM1 and AOM2 efficiently transmit their +1 and −1 first-order diffracted mode, respectively. A 1×2 fiber coupler is utilized to split the light out of the DFB laser, with the beam subsequently traversing its respective AOM. The two beams undergo frequency shifts of $\Omega_{+1} = -\Omega_{-1}$, of equal magnitude but opposite sign. Here the employed fiber technology turns out to be advantageous because the use of a 2×1 fiber coupler out of the AOMs enables both the up- and down-shifted beams to be recombined and merged into the same fiber mode. This arrangement allows efficient coupling into the same RDC transverse mode, namely the TEM_{00}. By the very nature of this setup, both beams sample the same spatial region of the multilayer surfaces of the RDC mirrors. The RF sources driving the AOMs are fine tuned to satisfy $\Omega_{+1} - \Omega_{-1} = 2 \times \mathrm{FSR}$ so that both beams can be simultaneously resonant with the same transverse mode of the RDC. This arrangement makes it possible to alternately measure intracavity losses associated with two different longitudinal RDC modes separated by this constant frequency difference.

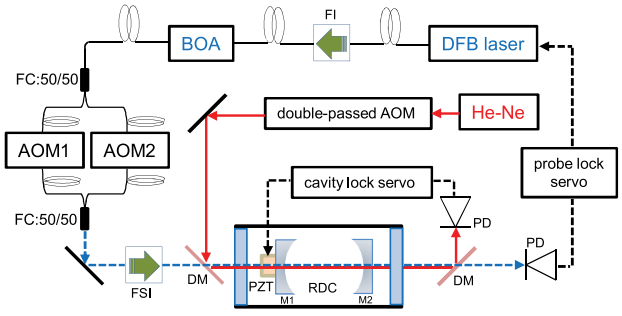

Fig. 1. Schematic diagram of the D-CRDS system. FI, fiber isolator; FSI, free space isolator; FC, fiber coupler; DM, dichroic mirror; PD, photodetector; BOA, booster optical amplifier; M1 and M2, RDC mirrors. The RDC length is stabilized through the cavity lock servo as detailed in [11]. The probe lock servo ensures that the two diffracted beams (from AOM1 and AOM2) are resonant with the RDC and allows for alternately switching these beams on and off.

Measurements of empty cavity base losses are shown in Fig. 2, where we illustrate advantages and potential pitfalls of the D-CRDS method introduced in this study. To this end we present two sets of data, shown in Figs. 2(a) and 2(b). The first of these corresponds to the etalon-immune distance corresponding to the photodetector position that minimizes the etalon amplitude, and the other corresponds to the position that amplifies the etalon. In Fig. 2(a) the probe beam photodetector has been installed 37 cm (namely $\sim l_c/2$) away from the MLS of M2, while in Fig. 2(b) this photodetector has been moved 55.5 cm away ($\sim 3l_c/4$) from the MLS of M2. As discussed above and as highlighted by the red curve depicted in Fig. 8 of the Appendix, these distances correspond to configurations where pairwise differencing the cavity modes with $\Delta q = 2$ either cancels out or doubles the amplitude modulation associated with etaloning. Both empty cavity spectra were acquired without user intervention by temperature tuning the DFB probe laser through successive cavity resonances. With the DFB laser locked to the RDC, 100 cavity decay time constants were acquired and averaged at each spectrum point. Each spectrum point required about 10 s, which included the time for ring-down decay signal acquisition, laser temperature tuning, and laser relocking.

Inspection of Figs. 2(1)(a) and 2(1)(b) reveals that the CRDS spectrum of base cavity losses exhibits oscillations with a period of ~25 GHz, which corresponds to an optical path length of 6 mm. We assign this etalon to spurious reflections from the unwedged back surfaces of the fused silica RDC mirrors (thickness ~4 mm, with $n = 1.44$ at $\lambda = 1.6$ μm). There also exists a faster oscillation arising from a spurious reflection at the surface of our detector. These two main sources of feedback to the RDC are clearly discernible in the fast Fourier transform (FFT) of the base loss measurements (not shown in Fig. 2) where, the optical frequency detuning $\Delta\nu$ is converted into equivalent etalon lengths through the relation $l_e = c/(2\Delta\nu)$. Comparison of Figs. 2(1)(a) and 2(1)(b) and 2(2)(a) and 2(2)(b) reveals that (depending on the position of the detector surface relative to the RDC) the D-CRDS method can either reduce [Fig. 2(a)] or amplify [Fig. 2(b)] the amplitude of the etalon seen in CRDS.

Coupled-cavities originate from interfaces traversed by the light in the setup. Of course, the relative importance of the respective contributions depends both on the intensity of the spurious reflection and the spatial coupling efficiency into the RDC transverse mode, cf. Appendix Eqs. (A1) and (A2). In our setup the most common external surfaces contributing to

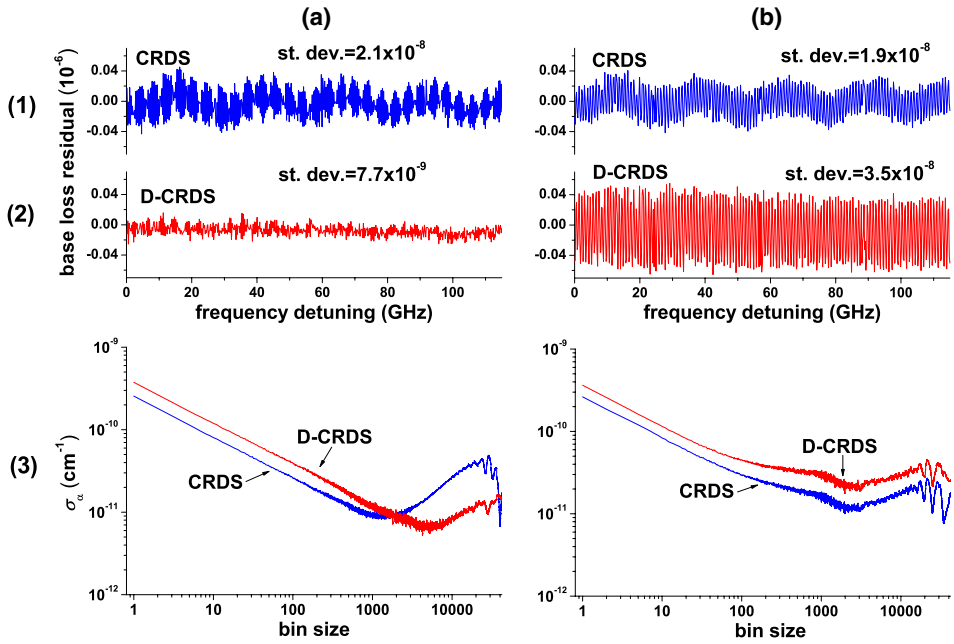

Fig. 2. Experimental comparison between two extreme cases for the $\Delta q = 2$, D-CRDS system. (a) The detector surface forms a source of feedback that is at a distance of $l_c/2$ from the MLS of M2 (i.e., amplification factor 0, cf. Fig. 8), while in (b) it has been placed at a distance of $3l_c/4$ from the same RDC mirror (i.e., amplification factor 2, cf. Fig. 8). Blue and red traces correspond to CRDS and D-CRDS measurements, respectively. In (1)(a) and (1)(b) we present the baseline-subtracted empty cavity losses $[l_c/(c\tau)]$ of the RDC obtained from the conventional CRDS method while in (2)(a) and (2)(b) we show the resulting D-CRDS measurements. Note that the same vertical scale has been used in (1) and (2) in order to highlight the importance of the ERRs characteristic of the D-CRDS technique. The horizontal axes represent the optical frequency detuning $\Delta\nu$. We assign the small slope in the D-CRDS spectrum to residual quadratic frequency dependence of the mirror losses. (3) shows the Allan deviation σ_α versus averaging bin size δ_b and related improvements in drift cancellation afforded by the differential technique when using a proper setup that minimizes the amplification factor. Measurement pairs were acquired at a rate of ~10 Hz, such that an averaging bin size of unity corresponds to a 100 ms averaging time.

etalons are the back sides of the RDC mirrors ($l_e \sim 6$ mm), the vacuum windows ($l_e \sim 13$ mm and $l_e \sim 18$ mm), the fiber end ($l_e \sim 85$ cm), and the surface of the detector itself. Note that this list does not include the mode-matching lens or the lens that focuses the RDC transmitted signal on the active surface area of the detector since their biconvex surfaces yield little specularly reflected light and small spatial coupling coefficients. Experimentally, we found it necessary to incorporate a free-space isolator in the setup between the single-mode fiber and the RDC. Indeed, we observed variations in τ as large as 10% that were caused by optical feedback from the fiber end to the RDC. This result is not surprising because by a time reversal symmetry argument the coupling efficiency of the returning light that is retroreflected by the fiber end should be the same as the coupling efficiency of the probe laser beam (which is close to unity) into the TEM_{00} of the RDC.

Most importantly for high-fidelity line shape studies, the D-CRDS method can reduce the amplitude of etalons and, thus, diminish their contribution to spectrum residuals. To quantify the short term time scales over which averaging tends to improve precision, we performed Allan variance [18] measurements of the ring-down time constants with the probe laser at a fixed optical frequency. The results are given in Figs. 2(3)(a) and 2(3)(b). Here we have plotted the Allan deviation, σ_α, in units of loss per unit length versus the averaging bin size δ_b (corresponding to 100 ms per point). These Allan deviation plots quantify the improvement in precision afforded by increased averaging time (proportional to δ_b) as well as the optimal averaging time (given by the time scale at the Allan variance minimum). Consistent with that of a random process, σ_α initially decays with $1/\sqrt{\delta_b}$ for all four cases. However, for small values of δ_b the two D-CRDS cases yield Allan deviations that are a factor of approximately $\sqrt{2}$ larger than the corresponding CRDS cases. This is because the D-CRDS analysis involves two uncorrelated ring-down time constant measurements per point as opposed to one for the CRDS case. In Fig. 2(3)(a), corresponding to the setup where feedback sources are installed in ERRs, the minimum detectable absorption coefficients are $\sigma_\alpha \sim 7 \times 10^{-12}$ cm^{-1} and $\sigma_\alpha \sim 9 \times 10^{-12}$ cm^{-1} for the D-CRDS method and the conventional CRDS method, respectively. The improved sensitivity for the D-CRDS relative to CRDS is enabled by the ability to average for longer times (~120 s for CRDS and ~500 s for D-CRDS), which compensates for the $\sqrt{2}$-fold larger Allan deviation of D-CRDS for small values of δ_b. The longer optimal averaging time for the D-CRDS case indicates a reduced sensitivity to drift in external etalons, which we ascribe to reduction in the etalon amplitude. Conversely, when the photodetector is placed at a position that amplifies the formation of an etalon, apart from the constant $\sqrt{2}$-fold vertical shift we find that the D-CRDS and CRDS Allan deviations are nearly identical.

A noteworthy attribute of the D-CRDS method is that one can quantitatively probe any transverse mode of the RDC. This is possible despite the fact that there are large transverse-mode-dependent variations in the ring-down time constants which are caused by nonuniformity in reflectivity across the surface of RDC mirrors. However, as discussed above, D-CRDS is insensitive to the base mirror losses because of the differencing nature of the technique. Consequently, the sampling density of acquired spectra could be

increased by combining measurements made on various transverse modes of the RDC. We note that although degeneracy splitting of non-TEM_{00} modes may occur because of mirror astigmatism, it has been shown that these signals can be readily modeled by biexponential decays [19].

We also performed measurements to verify that drift in the base losses could be ascribed to changes in the phase of an external etalon in accordance with Eq. (2). To this end, we monitored the cavity decay time over several hours, with the photodetector installed at $l_c/2$ and the laser frequency continuously locked to the stabilized RDC. We simultaneously recorded the laboratory barometric pressure p and air temperature T. Time series for these measurements are summarized in Fig. 3, where we show fractional variations in the measured and modeled base losses $1/(c\tau)$ (upper panel) as well as p and T (lower panel). These data were smoothed to reveal drift in the base losses. Notably, we found that the base losses correlated with air density and temperature. Specifically, it was possible to model this drift by incorporating two distinct mechanisms that affect the etalon phase: density-dependent changes in the refractive index of the laboratory air (p/T dependence), and thermal expansion of the optical table leading to changes in the geometric length of the etalon (T dependence). Details regarding the model are given in the caption of Fig. 3. Although the former mechanism for drift in ring-down base losses was previously discussed in [14], we are unaware of any previous analysis that explicitly

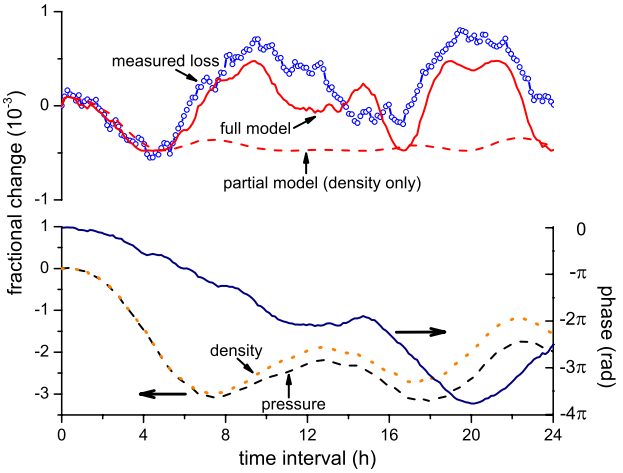

Fig. 3. Upper panel: measured (dashed blue line with open symbols) and modeled (solid and dashed red lines) fractional variation in RDC base losses, $1/(c\tau)$. Lower panel: the corresponding fractional variation in the measured air density and pressure (indicated dashed curves, left axis) and etalon phase (solid line, right axis). Fractional variations in the losses were modeled with the function $a_0[\sin(\phi_0 + (\phi - \phi_0) - \sin(\phi_0)]$ where $(\phi - \phi_0) = 4\pi\nu(n_0 l_0 - nl)/c$ assuming $\nu/c = 6250\ \mathrm{cm}^{-1}$ and an etalon of nominal length $l_0(T_0) = 40$ cm. Here changes in the etalon phase are calculated in terms of the measured air temperature and pressure (which alter the refractive index n of the laboratory air) and thermal expansion of optical table (which alters l). Air refractive index was calculated as $n - 1 = dn/d\rho\ \rho(p, T)$, with ρ being air number density and $dn/d\rho = 1.07 \times 10^{-23}\ \mathrm{cm}^3$ molecule-1. The temperature-dependent etalon length was modeled as $l(T) = l_0 + \beta(T - T_0)$, where β is the thermal expansion coefficient of stainless steel and assumed to be $1.69 \times 10^{-5}\ \mathrm{K}^{-1}$. The original sampling interval was ~8 min, and the data were smoothed to give an effective averaging time of ~7 h. The modeled loss included only the etalon amplitude, $a_0 = 4.8 \times 10^{-4}$ (corresponding to $\Delta\alpha_e = 1.3 \times 10^{-10}\ \mathrm{cm}^{-1}$), and the phase shift ϕ_0 as adjustable parameters.

considered thermal expansion effects. Inspection of Fig. 3 reveals that over the time interval 0–8 h, the fractional changes in the air density and pressure were nearly the same (indicating a nearly constant temperature). In this time interval, the first mechanism dominates (refractive index effect) and the model closely fits the observations. For longer times, the temperature begins to change enough (nominally 20 mK from the initial temperature) such that thermal expansion of the optical table affects the base losses. In this time interval, we found that the thermal expansion effect was necessary to ensure good agreement between the model and observations, and by eliminating it the model failed to capture the observed trend (partial model curve Fig. 3). Finally, as shown in the lower panel of Fig. 3, we found that the phase of the etalon changed by ~4π over the 24 h period, indicating that relatively long time scales can be required to average out the effects of drifting etalons.

C. Application to Measurements of Absorption Spectra

In order to demonstrate practical improvements achieved with the D-CRDS technique we probed the air-broadened rovibrational transition of CO_2 [R26e (30013←00001)] located near a wave number of 6246.3 cm^{-1}. These measurements were done on a dry gas sample (water vapor specified to be $<2\ \mu\mathrm{mol\,mol}^{-1}$) containing nominally 425 $\mu\mathrm{mol\,mol}^{-1}$ of CO_2 in air. A total of 98 spectra at a ring-down cell pressure of 13.3 kPa (100 Torr) and at room temperature were acquired. The total measurement time was ~33 h, corresponding to a single-spectrum acquisition time of nominally 20 min. Although the mode pairs were acquired at a nominal rate of 10 Hz, we note that the time required to temperature tune the DFB laser frequency was ~30 s. This process was rate limited by the time to break the probe laser lock and jump and relock to the next longitudinal mode of the RDC.

Measurement and fit results for single and averaged D-CRDS and CRDS spectra are given in Figs. 4(a) and 4(b), respectively. We fit both the Galatry profile (GP) and speed-dependent Nelkin–Ghatak profile (SDNGP) to the measured spectra using a nonlinear least-squares Levenberg–Marquardt algorithm [20]. Typical SDNGP fit results for the averaged spectra are displayed in the upper panels of Fig. 4 (solid lines). The physical basis and mathematical form for the GP and SDNGP profiles can be found in [21] and [22,23], respectively. The GP can be calculated in terms of the Doppler width Γ_D, the Lorentzian (collisional) width Γ_L and the narrowing frequency ν_n, whereas the SDNGP includes these three parameters, the pressure shifting parameter δ plus two speed-dependent terms given by a_w and a_s. Except for Γ_D and δ all other quantities were treated as fitted parameters. In the case of the SDNGP, we assumed a quadratic model for the speed dependence of the collisional broadening (B_w) and the speed dependence of the shifting (B_s) of the line [24], and these terms were approximated by $B_w(\eta) = 1 + a_w(\eta^2 - 3/2)$ and $B_s(\eta) = 1 + a_s(\eta^2 - 3/2)$, where η is the reduced absorber velocity as given in [25]. We set δ to the value given in HITRAN 2008 [26], which is equal to $-1.83\ \mathrm{kHz\,Pa}^{-1}$ ($-0.0062\ \mathrm{cm}^{-1}\,\mathrm{atm}^{-1}$). The differential line shapes $\Delta\alpha(\nu)$ measured were modeled as $\Delta\alpha(\nu) = \alpha(\nu + \Delta\nu) - \alpha(\nu - \Delta\nu) = n_a S(T)[g(\nu + \Delta\nu - \nu_0) - g(\nu - \Delta\nu - \nu_0)] + \Delta\alpha_b(\nu)$, where $\alpha(\nu) = (c\tau)^{-1}$, ν_0 is the line center, n_a is the absorber number density, $S(T)$ is the line intensity at the measurement temperature, and

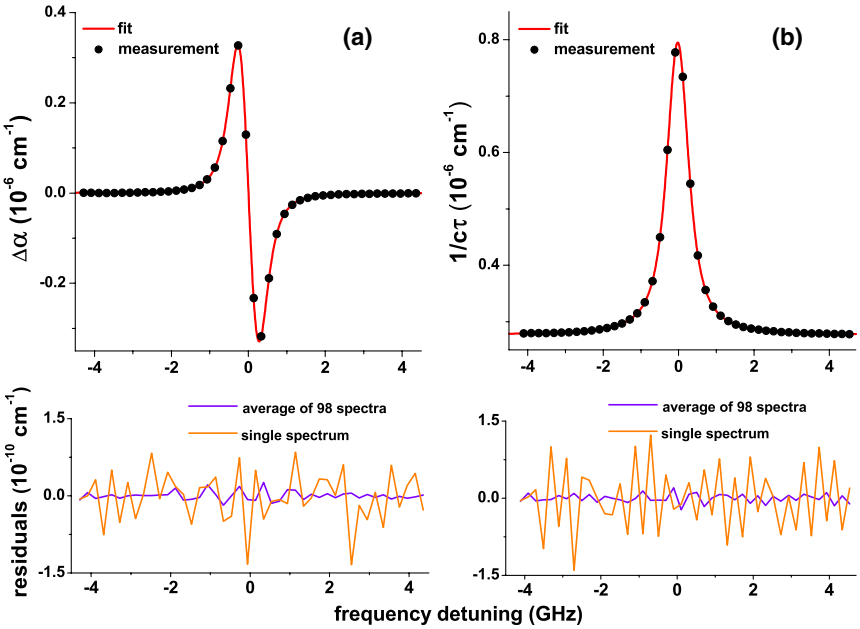

Fig. 4. Spectra (top) and fit residuals (bottom) of air-broadened CO_2 [R26e (30013←00001)] transition. (a) Two-channel D-CRDS spectrum and (b) conventional CRDS spectrum. These results were obtained by averaging 98 spectra. Lower panels: corresponding SDNGP fit residuals. Baseline rms values for single and average spectra, respectively, are: D-CRDS: 5.2×10^{-11} cm^{-1} and 3.9×10^{-12} cm^{-1}; CRDS: 6.9×10^{-11} cm^{-1} and 7.2×10^{-12} cm^{-1}.

$g(\nu - \nu_0)$ is the GP or SDNGP. The quantity $n_a\ S$, which corresponds to the peak area A_p for the conventional spectrum, also was treated as a fitted parameter. As given above, the quantity $\Delta\nu$ is half the frequency difference between mode pairs, given by $\Delta\nu = \Delta q \times (\mathrm{FSR})/2 = 201.057$ MHz. It also was necessary to include in the fitting procedure the quantity $\Delta\alpha_b(\nu)$, which accounts for the baseline losses of the differential spectrum. This term consists of two etalons and a residual baseline term.

We also compared the spectra obtained with D-CRDS to those measured via the single-channel CRDS measurements. To this end, the formula $\alpha(\nu) = n_a S(T) g(\nu - \nu_0) + \alpha(\nu_b)$ was fitted to the CRDS spectra, in which $\alpha(\nu_b)$ includes two etalons plus a baseline offset and slope and where the last term accounts for the weak wavelength dependence of the mirror reflectivity. We emphasize that compared to the CRDS case, fitting the D-CRDS spectra requires no additional spectroscopic parameters to model the intensity, position, and shape of the absorption line. With regard to the spectrum baseline, there are two etalons and a constant term for modeling both the CRDS and D-CRDS cases, whereas only the CRDS spectrum model includes a sloping baseline.

In the bottom panels of Fig. 4 we also show the SDNGP fit residuals for single and averaged spectra obtained by both techniques. The D-CRDS spectra exhibited lower root-mean-square (rms) residuals than the conventional CRDS results, and for the former case line shape deviations were manifest in the residuals more clearly. All things being equal and for uncorrelated baseline noise, the rms of the differential spectrum residuals is expected to be $\sqrt{2}$ times greater than that of the conventional spectrum given that the former requires twice as many observations as the latter. We confirmed this assumption by numerically simulating and fitting "noisy" spectra for the differential and conventional cases. Moreover, we also found for all parameters that the fit uncertainties of these simulated spectra were nominally a factor of $\sqrt{2}$ times greater for the differential case. However, analysis of our measured spectra yielded similar fitted parameter uncertainties for the differential and conventional measurements. We also found that the rms values of the differential spectra residuals were typically smaller than the conventional ones. We attribute the improved performance of the differential measurements to the reduction of etaloning (period of 400 MHz) in the baseline spectrum. Further, when comparing the differential and conventional measurements, all fitted quantities generally agreed to within the combined uncertainties of their fitted values. However, because all spectra were acquired at a single pressure, it was not possible to disentangle correlations between the fitted narrowing frequency ν_n and the speed dependent term a_w. We note that multispectrum fits acquired over a range of pressure are typically required to overcome this complication [27]. Nevertheless, fitting the GP to both the differential and conventional data yielded a narrowing coefficient, $\nu_n/p = 6.47(16)$ kHz Pa^{-1}. This result is similar to previous FS-CRDS measurements of the [R16 (30012←00001)] CO_2 line at 6359.9673 cm^{-1}, which gave ($\nu_n/p = 6.18(21)$ kHz Pa^{-1}) [27] and slightly larger than calculations based on molecular diffusion (5.44(27) kHz Pa^{-1}). We also obtained a broadening coefficient $\Gamma_L/(2p) = 20.39(8)$ kHz Pa^{-1} (temperature corrected to 296 K) that was nominally 2% below the HITRAN 2008 value [26], as was the case for previous FS-CRDS measurements of the 6359.9673 cm^{-1} CO_2 transition [27].

An important question that we considered is whether or not single-channel results (i.e., spectra obtained from single-channel measurements that are converted into differential spectra by calculating the pairwise differences between modes) give the same results as differential spectra obtained with the two-channel D-CRDS technique. In other words, we investigated whether differential spectra acquired in rapid succession with two distinct probe laser beams were the same as those obtained by a post-experimental subtraction of mode

pairs for a single channel. The most important difference between the two approaches is the characteristic time scale over which the mode pairs are acquired. In the two-channel D-CRDS case this time interval is the reciprocal of the ring-down acquisition rate, ~100 ms, whereas in the single-channel D-CRDS case the time difference is ~60 s. In Fig. 5, we compare these techniques as a function of number of averaged spectra n_s, illustrating that these approaches do indeed yield different results. Here, we introduce two figures of merit to compare the two-channel (fast) and single-channel (slow) D-CRDS results as well as conventional CRDS measurements. These quantities are the SNR displayed in Fig. 5(a), and the quality of fit (QF) in Fig. 5(b). Both are shown as a function of number of averaged spectra for all three cases. The SNR and the QF are computed as the ratio of absorption signal amplitude α_{amp}, [which equals $(\alpha_{max} - \alpha_{min})$ for the conventional CRDS spectra or equivalently $(\Delta\alpha_{max} - \Delta\alpha_{min})$ for the D-CRDS spectra] to either the rms of the random noise in the residuals of the spectrum baseline for the SNR or the rms of all the fit residuals for the QF [8]. The QF quantifies not only the random noise of the fit residuals but also all systematic differences between the measured line shape and the fitted line profile.

Figure 5(a) illustrates that the two-channel D-CRDS method gives the highest SNR for a given number of averaged spectra and, unlike the single-channel D-CRDS and CRDS cases, the SNR scales on average with the square root of n_s as would be expected for ergodic statistical behavior. The SNR for a single spectrum is higher for the two-channel D-CRDS case (~13,700) than for the CRDS case (~8300), and the averaged differential spectra yield a maximum SNR reaching ~170,000:1. The SNR and QF are similar for the CRDS case because the fit residuals are dominated by noise in the baseline, which masks systematic residuals in the fitted profile. Conversely, for the D-CRDS case, lower baseline noise increases the relative importance of residuals under the absorption peak, thus reducing the QF relative to the SNR.

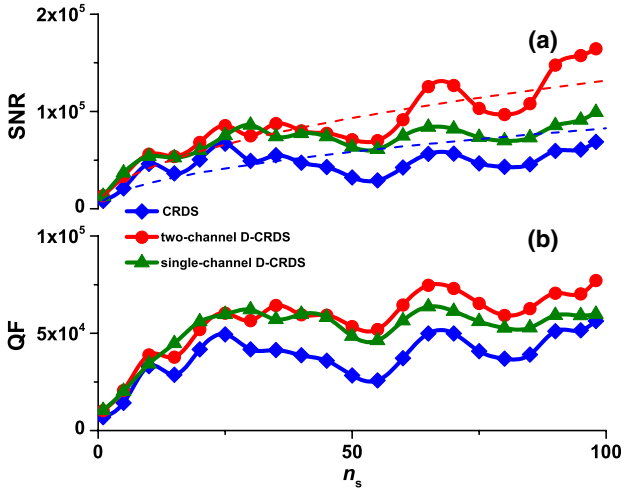

Fig. 5. (a) SNR versus number of averaged spectra n_s, obtained for CRDS for two-channel D-CRDS and single-channel D-CRDS spectra. Dashed lines indicate calculated values given by the square root of the number of averaged spectra times the corresponding average SNR obtained for single spectrum. (b) QF versus number of averaged spectra for the differential and conventional spectra. Data points are connected with spline fits.

We attribute the improved SNR of the fast two-channel D-CRDS measurements (compared to those of the slow single-channel case) to more efficient suppression of time-dependent etalons. This value of SNR corresponds to a minimum detectable absorption coefficient of 4×10^{-12} cm^{-1} and is comparable to recently reported line shape measurements of O_2 with a Pound–Drever–Hall-locked FS-CRDS system [8]. Although our results were acquired over a similar time scale, we achieved this result with ~10 times fewer spectra than reported in this previous study. Assuming ergodic improvement in the measurement precision, equal averaging times, and accounting for the differences in the base cavity losses, our minimum detectable absorption coefficient is consistent with recent measurements that used an unstabilized and dithered RDC [7], although we note that the latter system is not suitable for high-fidelity studies of molecular line shape.

For all three cases and for small values of n_s we find in Fig. 5(a) that the QF increases with n_s. As with the SNR, the highest QF is obtained for the two-channel D-CRDS spectra and on average the lowest QF occurs for the conventional CRDS spectra. We observe that for all three cases, the QF has two local minima, which occur for $n_s \sim 55$ and ~80. This effect is likely caused by incomplete compensation of etaloning in the data analysis. This is consistent with previous observations that revealed the importance of considering additional etalons in the analysis of long-term averaged FS-CRDS spectra [8]. It can be seen clearly in Fig. 5 that both D-CRDS realizations reduce the depth of the minima occurring at $n_s = 55$ averaged spectra, whereas the relative depth of the CRDS case remains approximately constant. Depth reduction of the first minimum is consistent with reduction in the etalon amplitude, which is afforded by the D-CRDS technique. The approximately constant depth of the second minimum suggests that it is caused by an etalon, whose amplitude is neither significantly reduced nor amplified for $\Delta q = 2$ (see Appendix Fig. 8).

We also emphasize that the amplitudes of the differential and conventional spectra do not have the same pressure dependence. This property is illustrated in Fig. 6(a) where the ratio of the peak absorption for the differential to

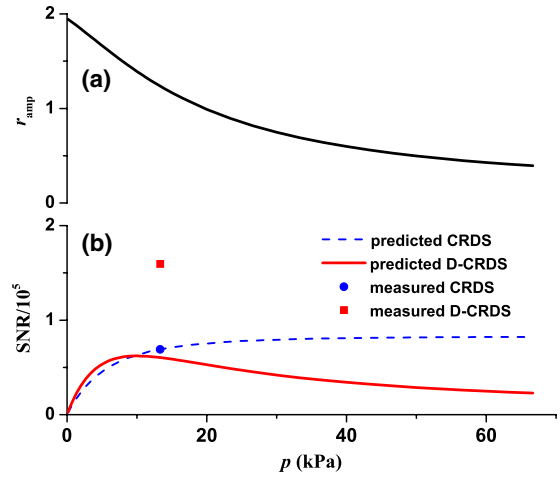

Fig. 6. (a) Calculated absorption amplification factor r_{amp} as a function of pressure. (b) Spectrum SNR as a function of pressure for the air-broadened CO_2 [R26e (30013←00001)] transition. The two symbols labeled "measured" correspond to the maximum SNR values reported in Fig. 5. The curves labeled "predicted" are based on scaling the maximum measured CRDS value as discussed in the text.

conventional cases r_{amp} is shown as a function of pressure. As pressure is reduced r_{amp} tends to increase. At low pressure, the amplitude of the differential spectrum is eventually limited by the Doppler width and approaches a maximum value nearly twice that of the conventional spectrum, whereas for the absorption transition considered here both types of spectra have similar amplitudes when $p \sim 20$ kPa. In Fig. 6(b) we show the maximum measured SNR (corresponding to $n_s = 98$) for the conventional and differential cases (symbols) and predicted SNRs for these two cases (lines) as a function of pressure. The dashed line labeled "predicted CRDS" is based on the measured SNR value of the CRDS spectrum scaled by the calculated pressure dependence of the absorption signal. Similarly, the solid red line labeled "predicted D-CRDS" was calculated using the SNR for the predicted CRDS curve times the factor $r_{amp}/\sqrt{2}$. Consistent with our previous discussion, these results illustrate that our measured SNR for the differential spectra was more than 2.5 times greater than the predicted value, which we attribute to the reduction of etaloning in the spectrum baseline. These results indicate that the differential method should yield improved spectrum SNRs compared to conventional measurements over a relatively wide range of pressure.

3. CONCLUSIONS

We have demonstrated a cavity-enhanced absorption technique that reduces sensitivity to etalons that often modulate resonator base losses. Called D-CRDS, this method involves measurements of decay rates for pairs of modes that are separated by a fixed optical frequency. We anticipate that the D-CRDS analysis method can be exploited in CRDS experiments where the spectrum acquisition rate is fast enough to compensate for confounding effects of drifting etalons. For a rapidly scanned, single-channel cavity ring-down system this technique requires only a slightly modified approach to the data analysis. Furthermore, the high SNR and high QF obtained here indicate the potential for stringent tests of theoretical line profiles. In this context, the occurrence of poorly characterized etalons is often problematic in data reduction because fitting these background signals can bias fitted line shape parameters. The differencing method presented here provides a useful strategy that enables the efficient suppression of these insidious spectrum interferences.

APPENDIX A: COUPLED-CAVITY MECHANISM TO INDUCE ETALONING: GENERALIZATION

We recently presented an analysis for coupled cavities that models feedback from an external optical element to a high-finesse RDC [3]. We experimentally validated the predicted amplitude and phase of etalons that modulate the base losses of the RDC. Thus, we found that one can describe a coupled-cavity system by an equivalent two-mirror configuration in which the RDC mirror involved in the feedback has an effective reflectivity that is different from the isolated case. This effective reflectivity depends on the reflectivity of the isolated ring-down mirror and the position, reflectivity, and spatial coupling coefficient of the external optical element that recycles the light. In the following, we generalize the analysis to the case of N partially reflective interfaces that feed light back to the RDC as shown in Fig. 7. For this scheme, the light leaking out of the RDC is partially and successively further retroreflected by the set of optical interfaces labeled $1, 2, 3 \ldots N$ whose amplitude reflectivity and amplitude transmission are, respectively, denoted by $(r_{1,2,3\ldots N},\ t_{1,2,3\ldots N})$. Following the notation of Fig. 7 and neglecting absorption, we find an effective amplitude reflectivity for M1 of

$$r_{\mathrm{RDC,eff}} = r_{\mathrm{RDC}} + \frac{C_{00} r_1 t_{\mathrm{RDC}}^2 e^{2i\phi_1}}{-1 + e^{2i\phi_1} r_1 r_{\mathrm{RDC}}} \tag{A1}$$

for $N = 1$, and more generally,

$$r_{\mathrm{RDC,eff}} = r_{\mathrm{RDC}} + t_{\mathrm{RDC}}^2 \sum_{j=1}^{N} \frac{C_{00,j} r_j e^{2i\phi_j} \prod_{k=1}^{j-1} t_k^2}{(-1)^j + e^{2i\phi_j} r_j r_{\mathrm{RDC}} \prod_{k=1}^{j-1} t_k^2} \tag{A2}$$

for $N > 1$. Here $t_{\mathrm{RDC1}} = (1 - r_{\mathrm{RDC1}}^2)^{1/2}$ and $t_k = (1 - r_k^2)^{1/2}$ are the amplitude transmission of both the high-reflective MLS of the RDC mirror and the kth interface, respectively; $\phi_j = 2\pi l_j \lambda^{-1}$ is the single-pass phase shift experienced by the light while propagating through the jth coupled-cavity, which is a distance l_j from the involved MLS; and $C_{00,j}$ is the jth TEM_{00} amplitude coupling coefficient of the feedback beam associated with the jth coupled cavity (see [2] for further details). Of course identical relationships hold for M2.

From Eq. (A1), we can calculate the modified ring-down time constant in the case of self-mixing through both RDC mirrors M1 and M2 as $\tau_{\mathrm{eff}} = l_c/(cT_{\mathrm{RDC,eff}})$, where $T_{\mathrm{RDC,eff}} = 1 - (|r_{\mathrm{RDC1,eff}}^2| \times |r_{\mathrm{RDC2,eff}}^2|)^{1/2}$ represents the geometric mean transmittance of the RDC system and l_c is the distance between M1 and M2. As an illustration of the magnitude of the perturbation, we consider an RDC composed of two identical mirrors with an intensity transmission $T = 2 \times 10^{-5}$. If approximately 0.016% of the light that leaked through both RDC mirrors returns and constructively interferes with the circulating ring-down intracavity field (i.e., both returning fields maximize the effective reflectivity of the mirrors) and assuming

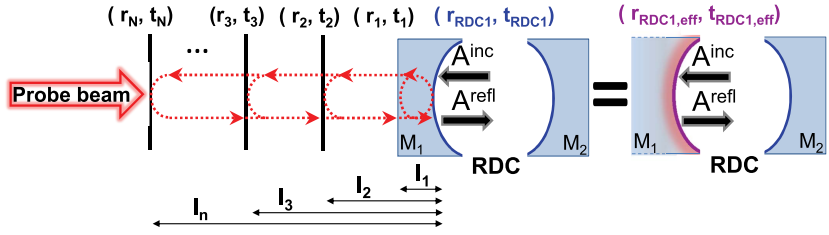

Fig. 7. Schematic diagram of a CRDS involved in a single-sided, coupled-cavity mechanism and its corresponding equivalent optical system. Once the probe-beam intensity has been interrupted, light leaks out of the RDC at a rate dictated by its round-trip losses. In the coupled-cavity case, the reflected field from the MLS of M1, given by A^{refl}, arises from the direct reflection of the RDC intracavity field $r_1 A^{\mathrm{inc}}$ plus the portion of all the circulating fields that retroreflects from the N interfaces and couples back into the RDC. Coupled-cavity effects alter the effective reflectivity of mirror M1 in the equivalent optical system, thus altering the base losses of the composite system.

$C_{00} = 1$ for both coupled cavities, then the resultant wavelength-dependent baseline losses would have a modulation amplitude of 10^{-6} or 5% of the isolated mirror transmission.

APPENDIX B: ETALON-REDUCED REGIONS (ERRS)

As illustrated in Fig. 2, sampling effects in D-CRDS must be taken into account in order to ensure that the differential technique tends to suppress and not enhance the etalon of interest. The sampling interval to which we refer is the D-CRDS differential frequency given by $\Delta q \times \mathrm{FSR}$. Consider a sinusoidal etalon whose amplitude is to be reduced. For the measurements reported here, it is clear that the FSR of the length-stabilized RDC intrinsically imposes a sampling grid on the acquired spectrum. Given that the D-CRDS technique relies on subtracting pairwise modes that are separated by this fixed frequency interval, one finds that the maximum difference in base losses obtained between neighboring modes that are separated by Δq should not exceed twice the amplitude of the original etalon. More specifically, an analysis of Eq. (2) (for the case of one etalon) shows that if the following inequality is satisfied

$$\frac{1}{\Delta q}\left(i-\frac{1}{6}\right) \le \frac{l_e}{l_c} \le \frac{1}{\Delta q}\left(i+\frac{1}{6}\right), \tag{B1}$$

then the differencing scheme will result in a sampled etalon having a smaller amplitude than that of the original etalon. Here $i = 0, 1, 2, \ldots, \infty$, l_e is the distance from the etalon-forming surface to the RDC mirror and l_c is the length of the RDC. Conversely, etalons associated with any coupled cavities whose lengths are out of these ranges will be increased in amplitude. We call these ranges (where the amplitude of the etaloning is effectively decreased by virtue of the differential analysis) the ERRs. Thus, retroreflecting optical elements in the D-CRDS setup must be installed within an ERR to reduce the effect of etaloning. Further, precise positioning of these items at a distance $i \times l_c/\Delta q$ away from the MLS of the RDC mirrors is necessary to ensure that the D-CRDS technique effectively suppresses the etalon background structure. In Fig. 8 we present the etalon amplification factor calculated from Eq. (2) as a function of l_e/l_c for $\Delta q = 1$, 2, and 3. This quantity varies between 0 and 2, and has Δq minima over the range $0 < l_e/l_c \le 1$. The ERRs have halfwidths of $1/(6\Delta q)$ and they are centered on minima that occur at values of l_e/l_c that correspond to multiples of $1/\Delta q$. Careful inspection of the amplification factor given in Fig. 6 reveals that its derivative is discontinuous at the minima. This is caused by a π phase shift of the differential etalon as the minimum is traversed. From Eq. (B1), we predict that the D-CRDS method in our system (where the two AOMs have been designed so that $\Delta q = 2$, with $l_c = 74$ cm) reduces coupled-cavity perturbations involving interfaces closer than ~6.2 cm from the MLS of the RDC mirrors and ranging from 30.8 to 43.2 cm, 67.8 to 80.2 cm, and 104.8 to 117.2 cm, etc.

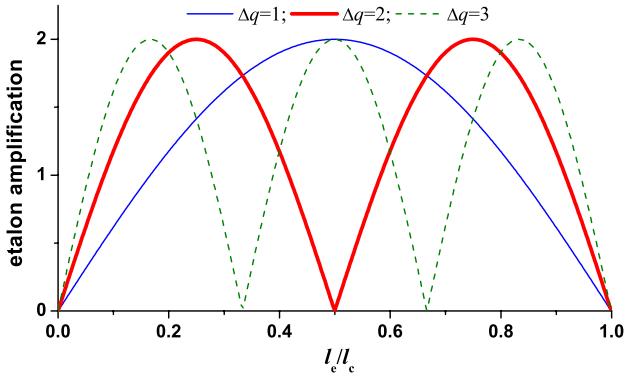

Fig. 8. Theoretical dependence of the etalon amplification factor on changes in the normalized etalon length for the first three differential systems.

ACKNOWLEDGMENTS

This research was supported by the National Institute of Standards and Technology (NIST) Greenhouse Gas and Climate Science Measurements Program. K. B. performed this research at NIST and was also partially supported by the National Laboratory FAMO in Toruń, Poland and the Foundation for Polish Science TEAM Project cofinanced by the EU European Regional Development Fund.

REFERENCES

1. J. Ye, L. S. Ma, and J. L. Hall, "Ultrasensitive detections in atomic and molecular physics: demonstration in molecular overtone spectroscopy," J. Opt. Soc. Am. B **15**, 6–15 (1998).
2. R. W. Fox and L. Hollberg, "Role of spurious reflections in ring-down spectroscopy," Opt. Lett. **27**, 1833–1835 (2002).
3. J. Courtois and J. T. Hodges, "Coupled-cavity ring-down spectroscopy technique," Opt. Lett. **37**, 3354–3356 (2012).
4. D. Romanini and K. K. Lehmann, "Ring-down cavity absorption-spectroscopy of the very weak HCN overtone bands with 6, 7, and 8 stretching quanta," J. Chem. Phys. **99**, 6287–6301 (1993).
5. S. Kassi, D. Romanini, A. Campargue, and B. Bussery–Honvault, "Very high sensitivity CW-cavity ring-down spectroscopy: application to the $a^1\Delta_g - X^3\Sigma_g^-(1)$ O_2 band near 1.58 μm," Chem. Phys. Lett. **409**, 281–287 (2005).
6. D. A. Long, D. K. Havey, M. Okumura, H. M. Pickett, C. E. Miller, and J. T. Hodges, "Laboratory measurements and theoretical calculations of O_2 *A* band electric quadrupole transitions," Phys. Rev. A **80**, 042513 (2009).
7. S. Kassi and A. Campargue, "Cavity ring down spectroscopy with 5×10^{-13} cm^{-1} sensitivity," J. Chem. Phys. **137**, 234201 (2012).
8. A. Cygan, D. Lisak, S. Wójtewicz, J. Domysławska, J. T. Hodges, R. S. Trawiński, and R. Ciuryło, "High-signal-to-noise-ratio laser technique for accurate measurements of spectral line parameters," Phys. Rev. A **85**, 022508 (2012).
9. P. W. Werle, P. Mazzinghi, F. D'Amato, M. De Rosa, K. Maurer, and F. Slemr, "Signal processing and calibration procedures for in situ diode-laser absorption spectroscopy," Spectrochim. Acta A **60**, 1685–1705 (2004).
10. P. Werle and S. Lechner, "Stark-modulation-enhanced FM-spectroscopy," Spectrochim. Acta A **55**, 1941–1955 (1999).
11. R. Grilli, G. Méjean, C. Abd Alrahman, I. Ventrilllard, S. Kassi, and D. Romanini, "Cavity-enhance multiplexed comb spectroscopy down to the photon shot noise," Phys. Rev. A **85**, 051804 (2012).
12. A. Foltynowicz, I. Silander, and O. Axner, "Reduction of background signals in fiber-based NICE-OHMS," J. Opt. Soc. Am. B **28**, 2797–2805 (2011).
13. A. O. O'Keefe and D. A. G. Deacon, "Cavity ring-down optical spectrometer for absorption-measurements using pulsed laser sources," Rev. Sci. Instrum. **59**, 2544–2551 (1988).
14. H. F. Huang and K. K. Lehmann, "Long-term stability in continuous wave cavity ringdown spectroscopy experiments," Appl. Opt. **49**, 1378–1387 (2010).

15. J. Ye and J. L. Hall, "Cavity ringdown heterodyne spectroscopy: high sensitivity with microwatt light power," Phys. Rev. A **61**, 061802 (2000).
16. D. A. Long, A. Cygan, R. D. van Zee, M. Okumura, C. E. Miller, D. Lisak, and J. T. Hodges, "Frequency-stabilized cavity ring-down spectroscopy," Chem. Phys. Lett. **536**, 1–8 (2012).
17. J. T. Hodges, H. P. Layer, W. W. Miller, and G. E. Scace, "Frequency-stabilized single-mode cavity ring-down apparatus for high-resolution absorption spectroscopy," Rev. Sci. Instrum. **75**, 849–863 (2004).
18. D. W. Allan, "Statistics of atomic frequency standards," Pr. Inst. Electr. Elect. **54**, 221–230 (1966).
19. H. Huang and K. K. Lehmann, "Noise in cavity ring-down spectroscopy caused by transverse mode coupling," Opt. Express **15**, 8745–8759 (2007).
20. D. W. Marquardt, "An algorithm for least-squares estimation of nonlinear parameters," J. Soc. Ind. Appl. Math. **11**, 431–441 (1963).
21. L. Galatry, "Simultaneous effect of Doppler and foreign gas broadening on spectral lines," Phys. Rev. **122**, 1218–1223 (1961).
22. B. Lance, G. Blanquet, J. Walrand, and J. P. Bouanich, "On the speed-dependent hard collision lineshape models: application to C_2H_2 perturbed by Xe," J. Mol. Spectrosc. **185**, 262–271 (1997).
23. D. Priem, F. Rohart, J. M. Colmont, G. Wlodarczak, and J. P. Bouanich, "Lineshape study of the $J = 3 \leftarrow 2$ rotational transition of CO perturbed by N_2 and O_2," J. Mol. Struct. **517**, 435–454 (2000).
24. J. Ward, J. Cooper, and E. W. Smith, "Correlation effects in theory of combined Doppler and pressure broadening—I. Classical theory," J. Quant. Spectrosc. Radiat. Transfer **14**, 555–590 (1974).
25. R. Ciuryło, "Shapes of pressure- and Doppler-broadened spectral lines in the core and near wings," Phys. Rev. A **58**, 1029–1039 (1998).
26. L. S. Rothman, I. E. Gordon, A. Barbe, D. C. Benner, P. E. Bernath, M. Birk, V. Boudon, L. R. Brown, A. Campargue, J. P. Champion, K. Chance, L. H. Coudert, V. Dana, V. M. Devi, S. Fally, J. M. Flaud, R. R. Gamache, A. Goldman, D. Jacquemart, I. Kleiner, N. Lacome, W. J. Lafferty, J. Y. Mandin, S. T. Massie, S. N. Mikhailenko, C. E. Miller, N. Moazzen-Ahmadi, O. V. Naumenko, A. V. Nikitin, J. Orphal, V. I. Perevalov, A. Perrin, A. Predoi-Cross, C. P. Rinsland, M. Rotger, M. Simeckova, M. A. H. Smith, K. Sung, S. A. Tashkun, J. Tennyson, R. A. Toth, A. C. Vandaele, and J. Vander Auwera, "The HITRAN 2008 molecular spectroscopic database," J. Quant. Spectrosc. Radiat. Transfer **110**, 533–572 (2009).
27. D. A. Long, K. Bielska, D. Lisak, D. K. Havey, M. Okumura, C. E. Miller, and J. T. Hodges, "The air-broadened, near-infrared CO_2 line shape in the spectrally isolated regime: evidence of simultaneous Dicke narrowing and speed dependence," J. Chem. Phys. **135**, 064308 (2011).